A&A 485, 753–763 (2008)
DOI: 10.1051/0004-6361:200809384

Astronomy
&
Astrophysics

An infrared-submillimeter study of starforming regions selected by the ISOSS 170 μm survey

M. Hennemann, S. M. Birkmann, O. Krause, and D. Lemke

Max-Planck-Institut für Astronomie (MPIA), Königstuhl 17, 69117 Heidelberg, Germany
e-mail: `hennemann@mpia.de`

Received 10 January 2008 / Accepted 7 April 2008

ABSTRACT

Context. Using the ISOPHOT Serendipity Survey (ISOSS) at 170 μm, a sample of galactic starforming regions has been established that exhibits very cold dust temperatures (<20 K) and high masses (>100 $M_\odot$).
Aims. We characterize the starforming content of five regions that were selected as potential sites of high-mass star formation in early stages.
Methods. We used SCUBA (JCMT) observations in the submillimeter to identify the dense condensations of cold gas and dust. Sensitive mid- to far-infared *Spitzer* observations with IRAC and MIPS allowed us to detect associated young stellar objects. From the long-wavelength emission we derived dust temperatures and masses for the identified clumps. A sample of associated mid-infrared sources is investigated using infrared color-color diagrams and the comparison to a model SED grid to constrain their evolutionary stages and derive estimates for additional parameters like the central mass.
Results. In every region, we identified between one and four submillimeter clumps with projected sizes between 0.1 and 0.4 pc. The dust temperatures range from 11.6 to 21.3 K and the estimated clump masses are 2 to 166 $M_\odot$. Towards the majority of submillimeter peaks, we found point sources in the near- to mid-infrared. Most are interpreted as low-mass young stellar objects, but we also detected very red sources. They probably represent very young and deeply embedded protostars that continue to accrete clump material and may reach higher masses. Several candidate intermediate-mass proto- or pre-main-sequence stars embedded in the clumps are identified.
Conclusions. A subset of four clumps may be massive enough (>100 $M_\odot$) to form high-mass stars and accompanying clusters. The absence of stellar precursors with current masses in the high-mass regime leave the type of star formation occurring in the clumps unsettled. We confirm the presence of large fractions of cold material as derived from large-scale far-infrared measurements that dominate the emission of most clumps and suggest that the starforming process will continue.

Key words. ISM: individual objects: ISOSS J19357+1950 – stars: formation – ISM: individual objects: ISOSS J19486+2556 – ISM: individual objects: ISOSS J20153+3453 – ISM: individual objects: ISOSS J20298+3559 – ISM: individual objects: ISOSS J22478+6357

1. Introduction

The origin of stars with masses of 10 $M_\odot$ or more is a lively issue. Only recently have approaches been presented to establish an evolutionary sequence based on observations and theoretical considerations (Beuther et al. 2007; Zinnecker & Yorke 2007). However, the observational basis for the earliest phases in the formation process of high-mass stars remains sparse, as many studies target luminous infrared sources revealing embedded stellar precursors associated with hot, as well as high-density, gas. Younger objects that are sometimes addressed as infrared-quiet massive cores should be best detected by far-infrared and submillimeter dust continuum surveys, as these cores are assumed to contain large amounts of cold material. Furthermore, the identification of extinction features against the galactic mid-infrared background provides a number of candidate objects commonly referred to as infrared dark clouds (IRDCs). Only a relatively small number of candidate sources have been investigated in detail (recently e.g. Beuther & Steinacker 2007; Rathborne et al. 2007; Birkmann et al. 2007), but results of larger-scale studies also suggest that the lifetimes of massive prestellar cores are very short (Motte et al. 2007).

The thermal emission from cold dust (<20 K) peaks in the wavelength range beyond the IRAS 100 μm limit. The 170 μm ISOPHOT Serendipity Survey (ISOSS) (Lemke et al. 1996; Bogun et al. 1996; Stickel et al. 2007) carried out during the ISO mission (Kessler et al. 1996) provides the first large-scale survey in this range and is well-suited to searching for extremely young and massive starforming regions. Selecting compact 170 μm sources ($FWHM < 3.5'$) that are associated with an IRAS 100 μm point source (Beichman et al. 1988) and molecular gas emission has led to the identification of a sample of more than 50 massive candidate sources (see Krause 2003; Krause et al. 2004, and references therein). The large-scale average dust temperatures derived from the flux ratios at 170 and 100 μm are about 18 K or lower, and the resulting mass-luminosity ratios are $M/L \sim 0.6\, M_\odot/L_\odot$, implying early stages in the process of star formation (cf. Sridharan et al. 2002). To explore the physical conditions in this unique sample of cold and massive starforming regions and to search for possible high-mass prestellar cores, a multi-wavelength follow-up survey was launched. The presence of very young massive clumps and cores has been confirmed for the regions ISOSS J20298+3559 (Krause et al. 2003), ISOSS J18364-0221 (Birkmann et al. 2006), and ISOSS J23053+5953 (Birkmann et al. 2007). In this paper we

Table 1. Observed ISOSS starforming regions.

Region ISOSS...	Assoc. IRAS point source	RA (J2000)	Dec (J2000)	Distance[a] in kpc	$T_{\rm FIR\,color}$[b] in K
J19357+1950	19335+1944	19:35:45.9	+19:50:58	4.0	17.5
J19486+2556	19465+2549	19:48:36.8	+25:56:55	2.9	18.0
J20153+3453	20134+3444	20:15:20.9	+34:53:53	2.0	19.0
J20298+3559	20278+3549	20:29:48.3	+35:59:24	1.8	16.0
J22478+6357	22460+6341	22:47:54.1	+63:57:11	4.1	15.4

[a] Kinematic distances obtained using the galactic rotation model of Brand & Blitz (1993) and identification of kinematically associated molecular cloud complexes (Krause 2003). [b] $T_{\rm FIR\,color}$ is derived from the far-infrared flux ratios at 100 μm (IRAS) and 170 μm (ISOSS).

report on observations of four more ISOSS starforming regions and extend the study of ISOSS J20298+3559.

Our continuum observations with high spatial resolution covering the submillimeter to near-infrared wavelength range allowed us to characterize the detailed starforming content. In the submillimeter we traced the thermal dust emission and identified compact condensations. To constrain their evolutionary stage, we conducted mid- and far-infrared observations using *Spitzer*. The long-wavelength data in the far-infrared and submillimeter was used to estimate the dust temperatures and total masses of the clumps. The sensitive mid-infrared data also revealed very young associated stellar objects. Additional deep near-infrared images provided a good assessment of source confusion. For the detected young stellar objects (YSOs), we performed an evolutionary classification from their infrared colors. In the Discussion section we then characterize a subset using radiative transfer models.

2. Observations, data reduction, and analysis

2.1. Submillimeter continuum emission

Submillimeter continuum jiggle maps at 450 μm and 850 μm were obtained with SCUBA (Holland et al. 1999) at the James Clerk Maxwell Telescope (JCMT) in July 2001 and May 2003 under good atmospheric transmission conditions ($\tau_{850\,\mu\rm m} \lesssim 0.2$). Reduction used the ORAC-DR (Jenness & Economou 1999) and SURF (Jenness & Lightfoot 1998) software. Photometric calibration was based on maps of Uranus acquired shortly before or after the observations. Further analysis used the MIRIAD (Sault et al. 1995) software package and followed the procedure described in Sandell & Weintraub (2001). To account for the deviations in the JCMT beam from a single Gaussian, we used the Uranus maps to construct symmetric beam models and deconvolve the maps of the target regions. The derived beam sizes are 7.8–8.8″ at 450 μm and 14.7–15.1″ at 850 μm. The maps were then restored using Gaussians of 8″ and 14″, respectively. By fitting Gaussian components to the restored maps, we first derived submillimeter continuum fluxes and deconvolved source sizes at 450 μm. We then used these sizes convolved with the 14″ Gaussian to extract 850 μm fluxes in order to only include emission from the same regions. The photometric accuracy is estimated to be 30% at 450 μm and 20% at 850 μm and the pointing uncertainty of the submillimeter maps is 2″ rms.

2.2. Near-infrared emission

Near-infrared images in J, H, and Ks were taken with the Calar Alto 3.5 m telescope using the two prime focus wide field cameras Omega2000 (Baumeister et al. 2003) and OmegaPrime (Bizenberger et al. 1998). Omega2000 features a field of view (FOV) of 15.4×15.4 arcmin^2 with a pixel scale of 0.4496″ pix^{-1}, while the FOV for OmegaPrime is 6.8×6.8 arcmin^2 with a pixel scale of ~0.4″ pix^{-1}. The exposure time in the broad band filters was 20 min each. The exposures were dithered on source to allow for sky subtraction. The reduction and photometry was done with IRAF (Tody 1993) and GAIA[1], and the photometric calibration for *J*, *H*, and *Ks* is based on the 2MASS point source catalog.

2.3. Mid- and far-infrared emission

The *Spitzer* (Werner et al. 2004) observations included IRAC (Fazio et al. 2004) imaging in all four photometric bands, MIPS (Rieke et al. 2004) imaging at 24 μm and 70 μm and the MIPS spectral energy distribution (SED) mode. For the imaging observations, the basic flux-calibrated data (BCD) of the *Spitzer Science Center* (SSC) pipeline was used for further data reduction and analysis. The calibration uncertainties of the data are about 2% for IRAC (Reach et al. 2005), 4% for MIPS 24 μm (Engelbracht et al. 2007), and 10% for MIPS 70 μm (Gordon et al. 2007). Cosmetic corrections and astrometric refinement were performed with the MOPEX software (Makovoz & Marleau 2005), and final images were combined using scripts in IRAF. Aperture photometry and PSF fitting was done with the aperture corrections given on the SSC website[2]. The MIPS SED mode calibration is based on a spectrum of α Boo (Low et al. 2005) and the measured MIPS 70 μm fluxes. The resulting photometric accuracy is estimated to be 5% (IRAC), 10% (MIPS 24), and 20% (MIPS 70 and SED).

3. Observational results: submillimeter emission morphology and associated mid-infrared sources

The five ISOSS regions are listed in Table 1 and displayed in Figs. 1 to 5. In the following we describe their individual submillimeter morphologies and point out the associated 24 μm sources. On the IRAC and near-infrared maps, those sources are marked for which singular counterparts can be identified at shorter wavelengths.

3.1. ISOSS J19357+1950

In this region three submillimeter emission components are resolved at 450 μm, two adjacent parts (SMM1 North and South) and a southwestern part (SMM2) (Fig. 1). They have deconvolved *FWHM* sizes of about 19″, 16″, and 20″, which correspond to 0.31–0.39 pc. An arc-shaped extended emission feature

---

[1] `http://star-www.dur.ac.uk/~pdraper/gaia/gaia.html`

[2] `http://ssc.spitzer.caltech.edu`

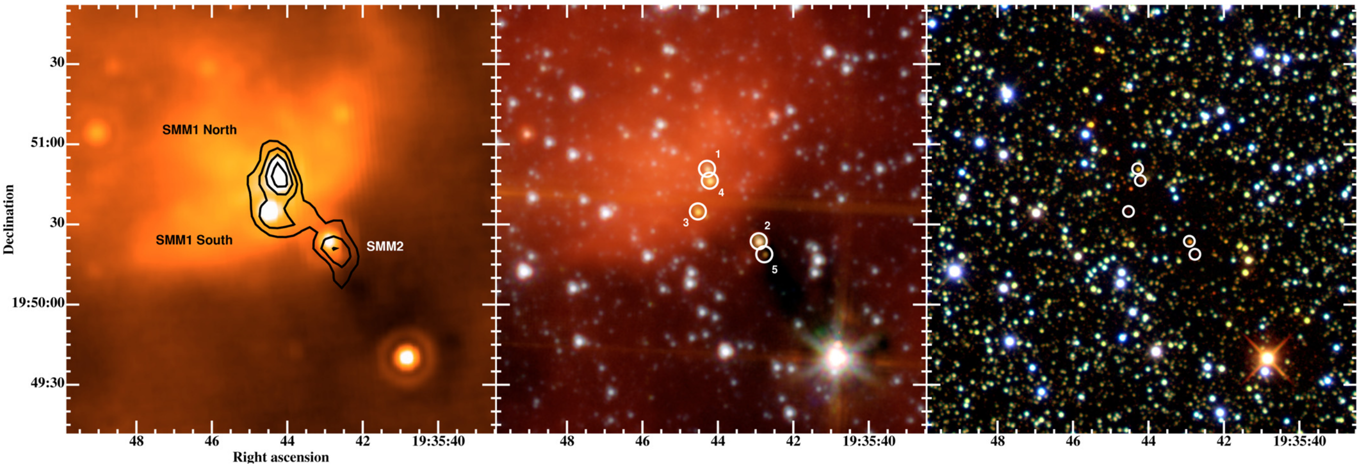

Fig. 1. Observations of the region ISOSS J19357+1950. *The left panel* shows the 24 μm map and the overlaid contours show the SCUBA 450 μm emission. *The mid panel* shows a color composite of the IRAC images. *The right panel* is a *JHK*s color composite using OmegaPrime and Omega2000 observations. The circles surround the sources investigated in the Analysis section.

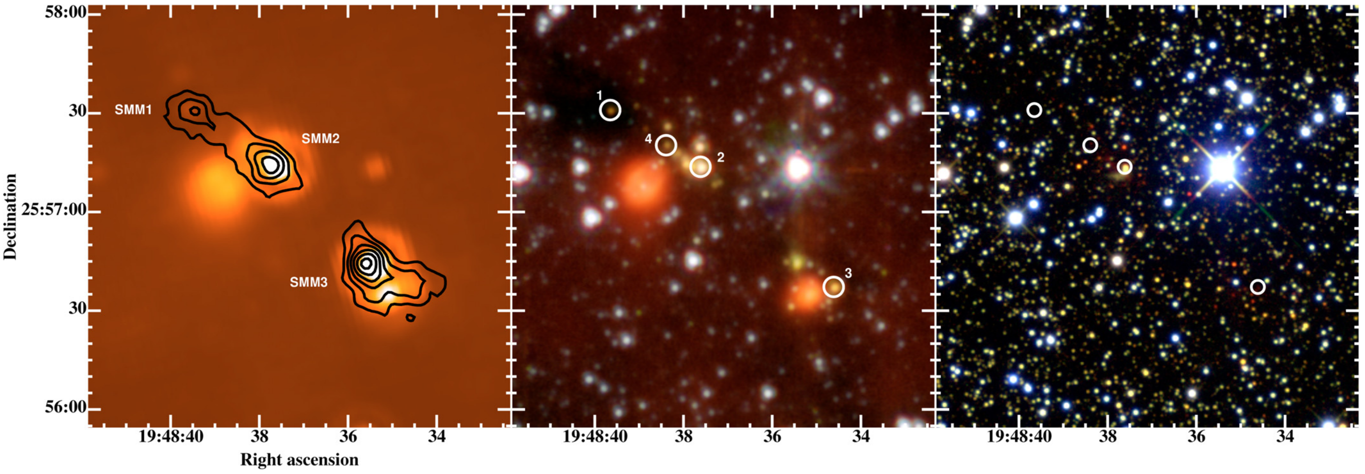

Fig. 2. Observations of the region ISOSS J19486+2556. Same arrangement and symbols as in Fig. 1.

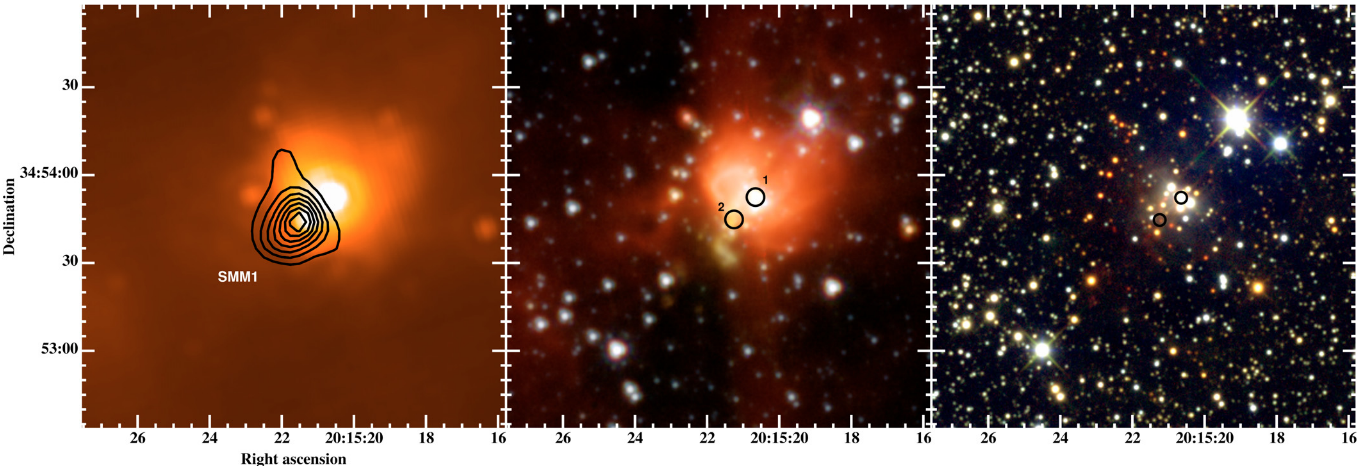

Fig. 3. Observations of the region ISOSS J20153+3453. Same arrangement and symbols as in Fig. 1.

that stretches from southeast to northwest is visible at 24 μm. Two 24 μm point sources are detected associated with SMM1 North. For SMM1 South and SMM2 one and two sources are present. Both SMM1 North and South are also coincident with emission at 70 μm but are not resolved individually. At the location of SMM2, no distinct 70 μm feature is detected.

3.2. ISOSS J19486+2556

Three submillimeter clumps are detected in this region. They are located along a chain from northeast to southwest and termed SMM1 to SMM3 (Fig. 2). All three appear compact in the submillimeter: The deconvolved *FWHM* diameters are

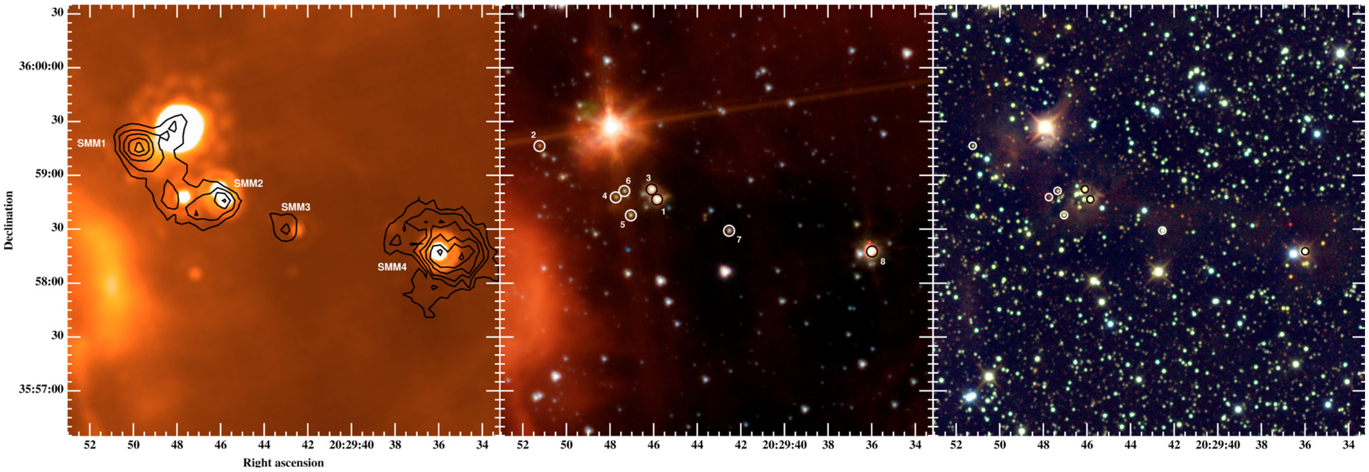

Fig. 4. Observations of the region ISOSS J20298+3559. *The left panel* shows the 24 μm map and the overlaid contours show the SCUBA 450 μm emission (for SMM3 the 850 μm emission is shown). *The mid panel* shows a color composite of the IRAC images. The right panel is a *JHK*s color composite using OmegaPrime and Omega2000 observations. The circles surround the sources investigated in the Analysis section.

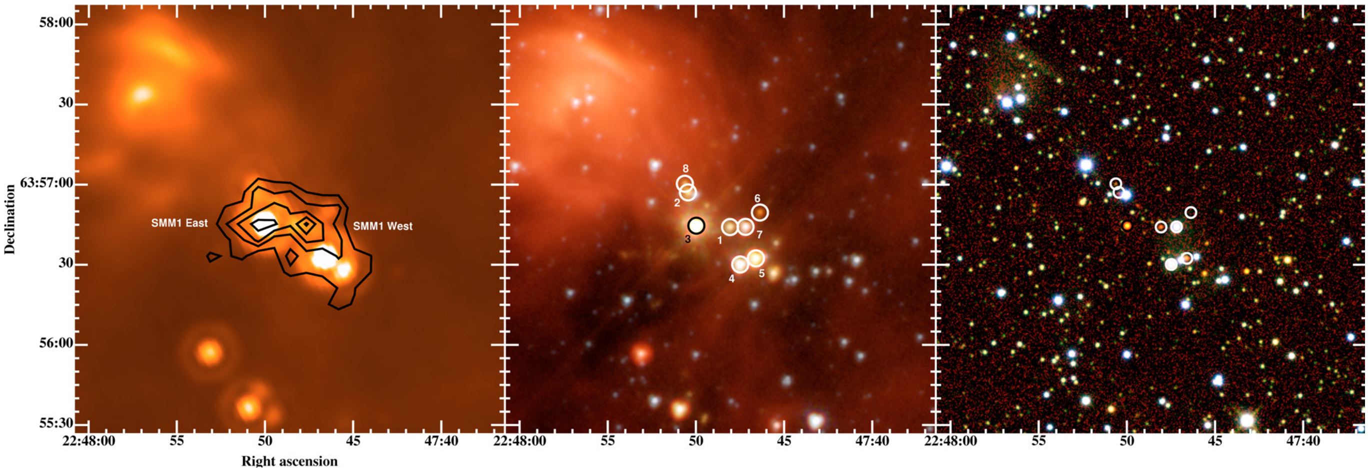

Fig. 5. Observations of the region ISOSS J22478+6357. Same arrangement and symbols as in Fig. 1.

about 16″ (SMM1), 10″ (SMM2) and 15″ (SMM3) at 450 μm. The corresponding length scales are 0.14–0.22 pc. Both SMM2 and SMM3 are associated with bright 24 and 70 μm sources. In the case of SMM2, several objects are detected at 24 μm, and the brightest one coincides with the submillimeter peak, as well as with the 70 μm source. For SMM3, one source at 24 and 70 μm is located at the submillimeter peak. In addition, two areas of extended 24 and 70 μm emission are found, one southeast of SMM2 and a second one towards the southern rim of SMM3. The first one is not associated with submillimeter emission. Only a faint source at 24 μm is detected towards the center of SMM1 and it is not associated with compact 70 μm emission.

3.3. ISOSS J20153+3453

This region contains a single submillimeter clump clearly detected in both SCUBA bands (Fig. 3). The deconvolved 450 μm *FWHM* extension is about 18″ × 14″, i.e., the projected diameter of the clump is around 0.16 pc. In the 24 μm band, two point-like sources surrounded by extended emission are detected towards the northwestern limb of the submillimeter clump. The brighter one is located among a cluster of sources seen at shorter wavelengths. None of these are resolved individually at 70 μm, but they instead blend into a single slightly extended source. The submillimeter emission peak is offset from the brighter point source by 11″.

3.4. ISOSS J20298+3559

This region has been studied in detail in Krause et al. (2003). Four submillimeter emission peaks are found in this region. Two of them are joined by extended emission (SMM1 and SMM2), while SMM3 and SMM4 are offset to the west (Fig. 4). SMM4 was not discussed in Krause et al. (2003). The sizes of the clumps SMM1 and SMM3 are approximately 0.14 and 0.17 pc, SMM2 is unresolved (<0.07 pc), and SMM4 is more extended. The deconvolved *FWHM* diameter is roughly 39″ corresponding to 0.34 pc. SMM1, SMM2, and SMM4 are associated with emission at 70 μm, and SMM3 was not covered by our 70 μm maps. Two 24 μm point sources are detected towards SMM2 and one towards SMM4. Both SMM1 and SMM3 have faint counterparts at 24 μm.

3.5. ISOSS J22478+6357

The submillimeter emission in this region traces an elongated clump (SMM1) that is resolved in both an eastern and a western component at 450 μm (Fig. 5). The deconvolved 450 μm

Table 2. Long-wavelength emission and derived properties of the cold component of the detected clumps.

Region ISOSS…	Clump	Total flux (Jy) 70 μm	93 μm	450 μm	850 μm	Size (pc)	Dust temperature (K)	Gas mass ($M_\odot$)
J19357+1950	SMM1 N	3.3	6.0	2.1	0.40	0.37	16.6–18.7	54–92
	SMM1 S	0.57	0.80–1.3^a	1.0	0.21	0.31	14.1–16.5	34–66
	SMM2	0.21	0.30–0.47^a	1.9	0.35	0.39	12.0–13.7	85–166
J19486+2556	SMM1	<0.15	<0.26	2.2	0.51	0.22	11.6–12.5^b	69–123^b
	SMM2	2.7	4.6	2.1	0.38	0.14	16.1–18.1	28–49
	SMM3	7.4	11	4.1	0.59	0.21	16.8–19.0	46–79
J20153+3453	SMM1	13	17	12	2.1	0.16	15.3–17.0	87–149
J20298+3559	SMM1	1.7	2.5–3.7^a	1.3^c	0.23^c	0.14^c	15.8–18.8^d	6–13^d
	SMM2	1.1	1.6–2.4^a	0.31^c	0.091^c	<0.07^c	17.3–21.3	2–3
	SMM4	0.41	0.81	3.9	1.0	0.34	12.1–13.2	46–80
J22478+6357	SMM1 E	0.80	1.6	1.0	0.35	0.14	14.7–16.4	47–81
	SMM1 W	0.72	1.0–1.6^a	1.8	0.47	0.24	13.4–15.5	79–153

^{a} Extrapolated values. ^{b} Derived using upper limit fluxes. ^{c} Flux values and sizes from Krause et al. (2003). ^{d} Derived from listed fluxes and 0.075 Jy at 1.2 mm (Krause et al. 2003).

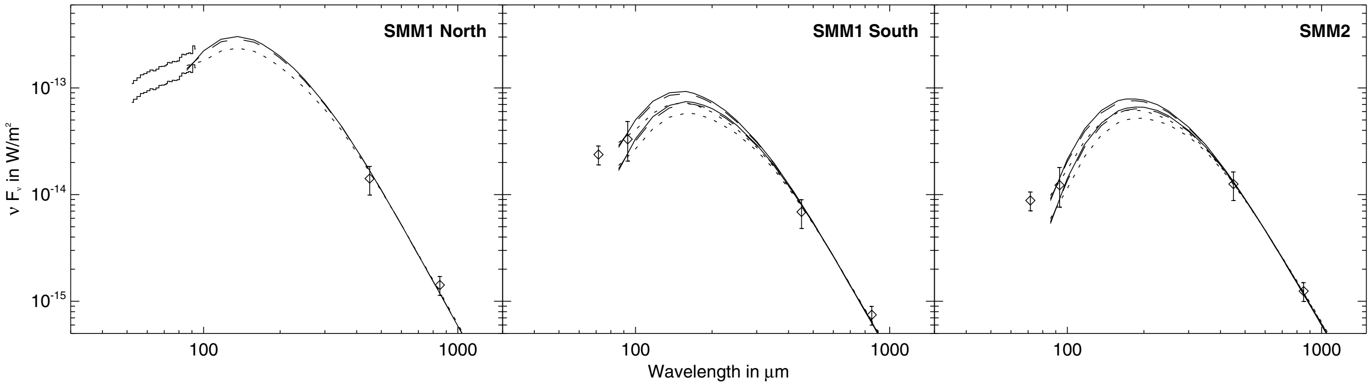

Fig. 6. Spectral energy distributions of the submillimeter sources in the region ISOSS J19357+2556. The diamonds represent photometric data obtained with MIPS (70 μm) and SCUBA (450 and 850 μm) and extrapolated data at 93 μm for SMM1 South and SMM2. Histogram-like bars show the error range of the MIPS SED spectrophotometry (53–93 μm) for SMM1 North. The lines show modified blackbody fits for $\lambda \geq 93\,\mu$m using different dust opacities (solid: no ice mantles; dotted: thick ice mantles; dashed: thin ice mantles). For SMM1 South and SMM2, two sets of curves are shown for spectral slopes of 0.3 and 2.0 in $70 \leq \lambda \leq 93\,\mu$m.

FWHM extensions of these are ~7″ and ~12″, corresponding to roughly 0.14 and 0.24 pc. At 24 μm, several point sources are associated. The brightest are located at the eastern and to the southern limb of the western submillimeter peaks. The 70 μm map reveals emission that coincides with the submillimeter peaks and with the 24 μm sources.

4. Analysis

We first present the analysis of the long-wavelength observations towards the starforming regions and then address the associated infrared sources. The extracted fluxes in the far-infrared and submillimeter are listed in Table 2. In Figs. 6–10 the spectral energy distributions (SEDs) of the detected clumps are sketched.

4.1. Far-infrared spectral slopes

The examination of the SEDs compiled for the seven detected clumps towards which MIPS SED observations were performed showed that the spectral slopes at wavelengths around 70 μm and below do not resemble a single thermal emission component that would reproduce the submillimeter fluxes. It presumably stems from warmer dust components or transiently heated very small grains (cf. Birkmann et al. 2007; Rawlings et al. 2005). The spectral slopes ($\mathrm{d}\log(\lambda F_\lambda)/\mathrm{d}\log\lambda$) vary in the range 0.3–2.0 for $70\,\mu\mathrm{m} < \lambda < 94\,\mu\mathrm{m}$.

4.2. Clump dust temperatures and masses

To characterize the cold component of dust (and gas) that gives rise to the emission at long wavelengths, we assumed that it can be reproduced by isothermal dust emission. As noted above, the fluxes at wavelengths around 70 μm and below do not conform to this assumption, so we used the datapoints at 93, 450, and 850 μm to estimate the dust temperature. In that respect we also assumed that the emission at these wavelengths is optically thin and can be approximated by a modified Planck spectrum. We used the dust opacities given in Ossenkopf & Henning (1994) for a MRN distribution either without ice mantles, with thin and with thick ice mantles ($\kappa_{850\,\mu\mathrm{m}} = 0.6$–$1.4\,\mathrm{cm}^2/\mathrm{g}$) corresponding to emissivity indices of $\beta = 1.81$–1.85 at long wavelengths. The dust-to-gas mass ratio is assumed to be 1/100. In the cases where no MIPS SED measurements are available, we extrapolated the 70 μm flux to 93 μm, allowing for spectral slopes of 0.3 and 2.0 (adopting the measured extremes). We list the resulting range of dust temperatures and gas masses for each clump in Table 2. The fitted curves are shown in Figs. 6–10.

4.3. Associated infrared sources

We detected a number of sources at 24 μm and shorter wavelengths that are associated with the submillimeter clumps. To evaluate their nature and relationship with the submillimeter

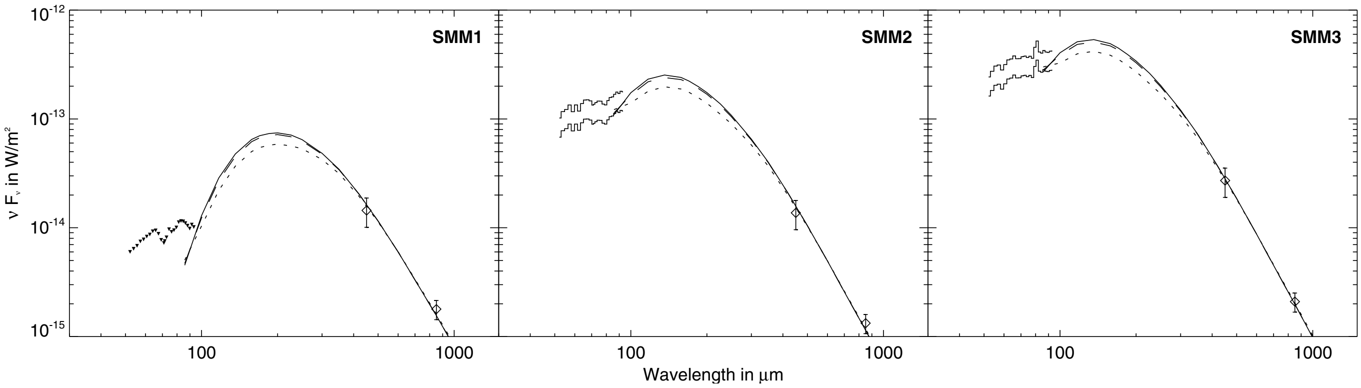

Fig. 7. Spectral energy distributions of the submillimeter sources in the region ISOSS J19486+2556. The diamonds represent photometric data obtained with SCUBA (450 and 850 μm). Histogram-like bars show the error range of the MIPS SED spectrophotometry (53–93 μm), upper limits for SMM1 are plotted with triangles. The lines show modified blackbody fits for $\lambda \geq 93\,\mu$m using different dust opacities (solid: no ice mantles; dotted: thick ice mantles; dashed: thin ice mantles).

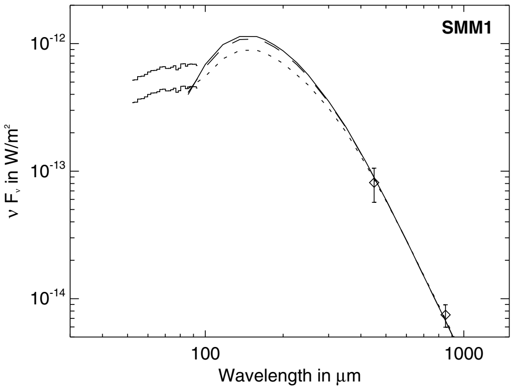

Fig. 8. Spectral energy distribution of the submillimeter source in the region ISOSS J20153+3453. The diamonds represent photometric data obtained with SCUBA (450 and 850 μm). Histogram-like bars show the error range of the MIPS SED spectrophotometry (53–93 μm). The lines show modified blackbody fits for $\lambda \geq 93\,\mu$m using different dust opacities (solid: no ice mantles; dotted: thick ice mantles; dashed: thin ice mantles).

condensations we selected the sources marked in the mid and right panels of Figs. 1 to 5, where we can identify singular counterparts. At distances of 2−4 kpc, the resolution achieved in the *K*s band corresponds to 1600−3200 AU and we could only probe the confusion of sources on larger scales than these. For sources that show no near-infrared counterpart, the IRAC resolution at 3.6 μm, which corresponds to 3000−6000 AU, limits the search for multiplicity. In addition we checked for optical counterparts in Second Digitized Sky Survey DSS2-red maps. Sources without optical counterpart are the best candidates to represent embedded objects, and therefore the association with the molecular and dusty clumps is presumably not a projection effect. However, the actual positions of the sources with respect to the clumps and the foreground extinctions are unknown.

Robitaille et al. (2006) present a grid of YSO model SEDs, which was used to analyze mid-infrared sources detected with *Spitzer* in starforming regions (Indebetouw et al. 2007; Shepherd et al. 2007). Utilizing a Monte-Carlo radiative transfer code, more than 20 000 2D models were computed for ten inclinations each. The different evolutionary phases in the modeled parameter space were ordered according to the Class system (André 1994) into stages: Stage 0/I (hereafter: Stage I) are very young objects that are deeply embedded in an extended envelope with a cavity surrounding an accretion disk, Stage II contains disk-dominated models, and Stage III represents star-dominated systems. Via a web interface, measured fluxes of individual sources can be put into a model SED-fitting routine to constrain source parameters (Robitaille et al. 2007), and we make use of this below in the Discussion section. The color-color diagram [3.6]–[5.8] versus [8]–[24] (Fig. 23 in Robitaille et al. 2006) offers a good distinction between the stages. These colors have also been compiled in Reach et al. (2004) for a number of YSOs in the Elephant Trunk Nebula, which have been classified before according to the Class system (see Reach et al. 2004, and references therein). For a verification of the color assessment, we plot their data and the regions corresponding to the stages proposed by Robitaille et al. (2006) in the upper left panel of Fig. 11. The foreground extinction appears to be small for these sources. The Class I/0 and I sources fall into the corresponding Stage I region with one exception. The colors of Class I/II and II sources lie in the Stage II region with one exception. The colors of the debris disk object β Pictoris place it on the border between the Stage II and III regions. These accordances support the utility of the colors for classification, so we applied this method to our source samples to get an estimate of their evolutionary status. However, due to the presence of a significant amount of dust in the regions, an enhanced extinction is expected for our sources. In the remaining five panels of Fig. 11, we plot the infrared colors of the sources that are marked (and numbered) in Figs. 1 to 5. Sources without an optical counterpart in DSS2-red maps are marked with crosses. Most of the evaluated sources exhibit colors lying in the Stage II region or in the vicinity of the Stage I/II transition. Interestingly, a few sources show very red colors that are consistent with Stage I even if a foreground extinction of $A_{\rm V} \geq 100$ is assumed. Exhibiting [8]–[24] > 5, these sources are distinct from the sample in the upper left panel. Two red sources, Source 1 in ISOSS J19486+2556 and Source 6 in ISOSS J22478+6357, apparently show enhanced 5.8 μm emission but still lie within the Stage I region. Both are very faint in the near-infrared.

Several sources are associated with "fuzzy" green features in the IRAC composite images and/or extended emission features in the near-infrared: Source 2 in ISOSS J19486+2556, Source 2 in ISOSS J20153+3453, Source 8 in ISOSS J20298+3559 and also towards the SMM3 peak in ISOSS J19486+2556, where we cannot identify the appropiate counterparts to the detected 24 μm source, and towards the SMM1 peak in ISOSS J20298+3559, where the 24 μm source shows no counterparts at shorter

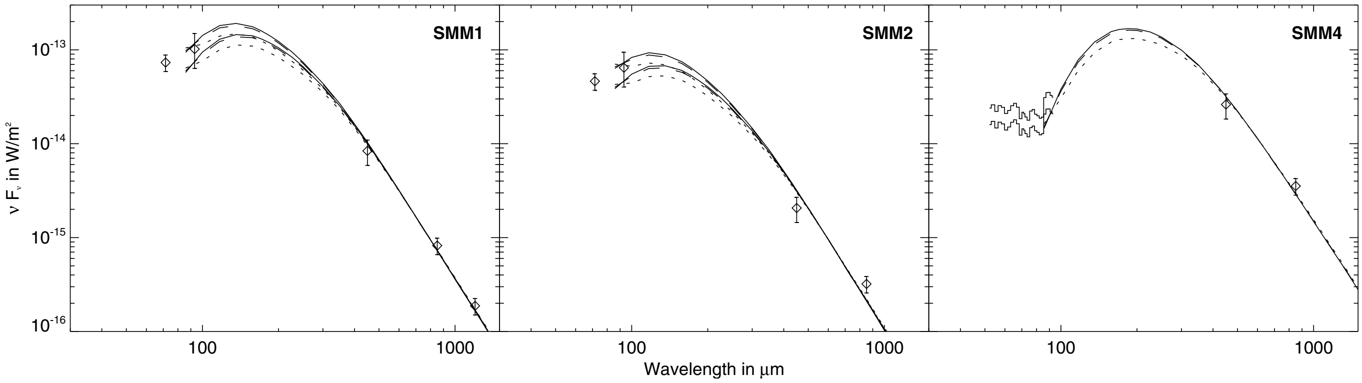

Fig. 9. Spectral energy distributions of the submillimeter sources in the region ISOSS J20298+3559. The diamonds represent photometric data obtained with MIPS (70 μm) and SCUBA (450 and 850 μm), extrapolated data at 93 μm for SMM1 and SMM2, and the datapoint at 1.2 mm for SMM1. Histogram-like bars show the error range of the MIPS SED spectrophotometry (53–93 μm) for SMM4. The lines show modified blackbody fits for $\lambda \geq 93\,\mu$m using different dust opacities (solid: no ice mantles; dotted: thick ice mantles; dashed: thin ice mantles). For SMM1 and SMM2 two sets of curves are shown for spectral slopes of 0.3 and 2.0 in $70 \leq \lambda \leq 93\,\mu$m.

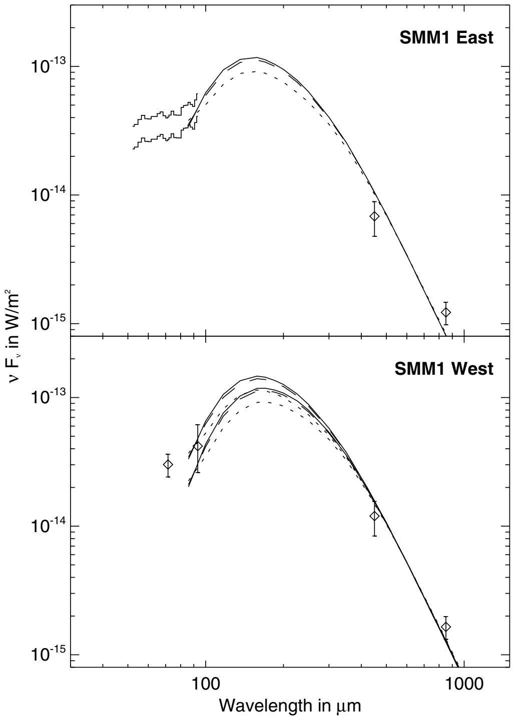

Fig. 10. Spectral energy distribution of the submillimeter sources in the region ISOSS J22478+6357. The diamonds represent photometric data obtained with MIPS (70 μm) and SCUBA (450 and 850 μm) and extrapolated data at 93 μm for SMM1 West. Histogram-like bars show the error range of the MIPS SED spectrophotometry (53–93 μm) for SMM1 East. The lines show modified blackbody fits for $\lambda \geq 93\,\mu$m using different dust opacities (solid: no ice mantles; dotted: thick ice mantles; dashed: thin ice mantles). For SMM1 West two sets of curves are shown for spectral slopes of 0.3 and 2.0 in $70 \leq \lambda \leq 93\,\mu$m.

wavelengths. These features probably trace outflow activity from young accreting objects, and this gives rise to shock-excitation of molecular hydrogen and CO. However, atomic hydrogen Br α line emission can also contribute to the IRAC 4.5 μm flux.

The most prominent features in the IRAC composite image of ISOSS J19486+2556 are two extended red emission features east of SMM2 and south of SMM3, which are also visible at the MIPS wavelengths. In the near-infrared very red objects are detected that are located towards the centers of the features that themselves are not traced. Extended low-density dust heated to higher temperatures could give rise to the mid- and far-infrared emission.

In the panel of Fig. 11 corresponding to ISOSS J20298+3559, we also plot the approximate colors of the brightest source in the region, located west of SMM1. It was investigated in detail in Krause et al. (2003) and classified as a Herbig B2e star that is accreting from a disk that is optically thick. The 8 and 24 μm images seem to show nonlinear effects due to the brightness of the source which may affect the derived colors corresponding to Stage II.

5. Discussion

5.1. The clump population

Our simple approach toward reproducing the long-wavelength emission of the sample of submillimeter clumps by one component neglects any effects of the density and temperature distributions within the clumps, and the assumption of optically thin emission may be violated in the far-infrared if the (column) density is high enough. Assuming a density profile that is flat in the innermost region of 100 AU radius, follows a power-law ($\rho \propto r^{-\alpha}$ with $\alpha = 1.5$) in between, and is cutoff exponentially at 20 000 AU, an optical depth of unity is reached at about 100 μm for a 100 $M_\odot$ condensation (dust opacities from Draine & Lee 1984; Steinacker, private communication). Therefore we may underestimate the total emission at the shortest wavelengths used (93 μm) and also the mean dust temperatures. Setting the dust temperature to a canonical value of 20 K results in a decrease in the mass by up to a factor of about two for the coldest temperatures, but would require high optical depths at wavelengths around 100 μm to be consistent with the measured fluxes. However, the required mass scales in the same way as the optical depth. It therefore seems unlikely that this effect causes errors in the mass estimation of more than a factor of two.

The distances to the regions are mainly derived from radial velocities and therefore carry some uncertainty. In Krause et al. (2003) the distance to ISOSS J20298+3559 was constrained by an extinction study to 1.8 ± 0.3 kpc. We estimate the other distances to be reliable within ~1 kpc, which results in possible mass changes by factors of 1.3 to 1.8. Another uncertainty factor on the order of two for the mass estimate arises from the unknown dust composition; e.g., the dust opacities given by

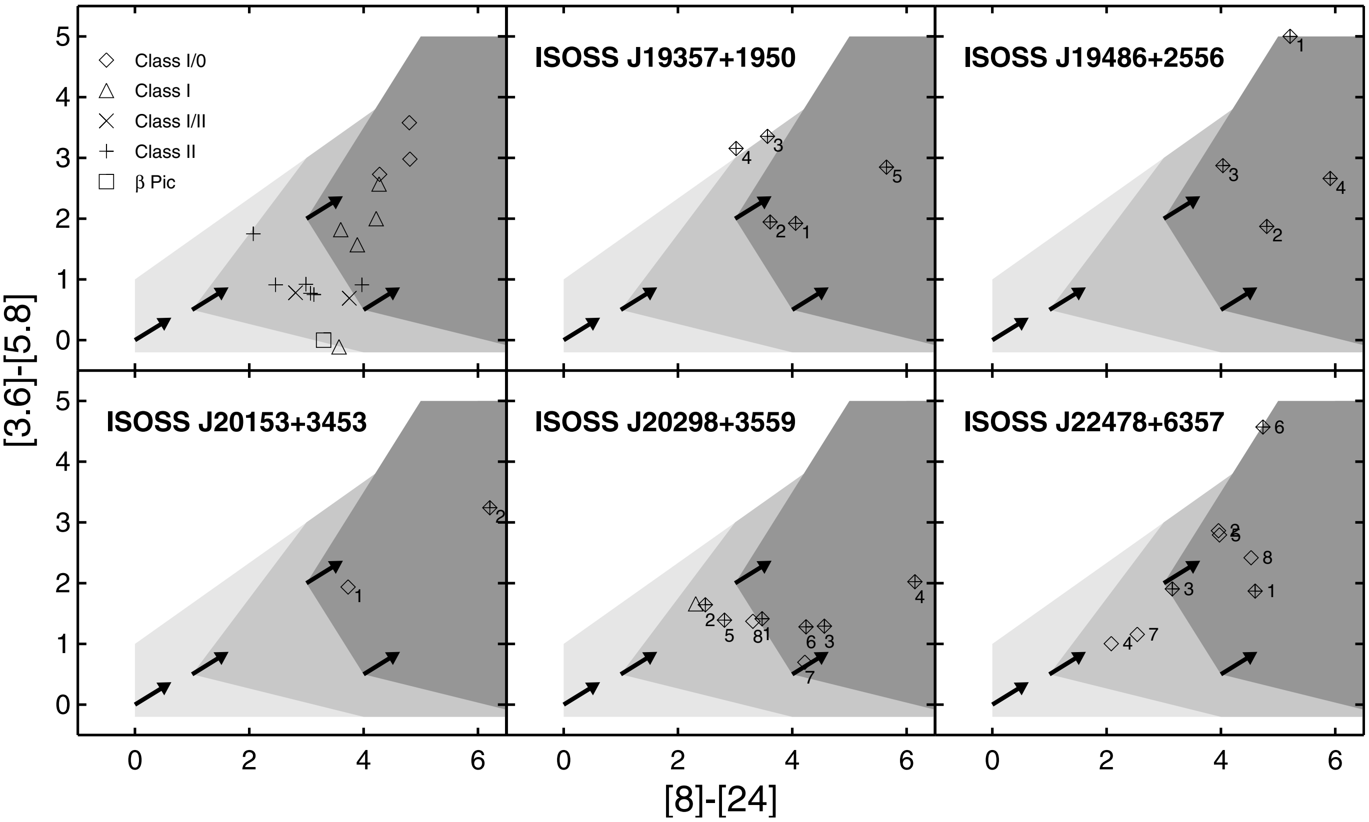

Fig. 11. IRAC and MIPS infrared color-color diagram. The regions where most models are Stages I, II, and III according to Robitaille et al. (2006) are shaded from dark to light grey. The vectors show an extinction of $A_V = 20$ (Indebetouw et al. 2005). In *the upper left panel*, young stellar objects corresponding to different evolutionary stages from Reach et al. (2004) are plotted. In the five remaining panels the mid-infrared sources associated with submillimeter emission in the ISOSS starforming regions are drawn (diamonds, numbering as in Figs. 1–5). The sources without optical counterpart are marked by crosses. In the panel corresponding to ISOSS J20298+3559, the approximate colors of the Herbig B2e star are represented by the triangle.

Ossenkopf & Henning (1994) are about five times higher than those used for calculating the model SED grid (Whitney et al. 2003). It is obvious from the SED diagrams that the dust models used in combination with the one-component approach does not fit the data well for all sources. In the cases of SMM2 in J20298+3559 and SMM1 East in J22478+6357, it seems that dust models corresponding to a lower value of the emissivity index β at long wavelengths or the introduction of several emission components would improve the fit. However, the latter approach would increase the number of variable parameters for the fit above the number of datapoints used. From the available measurements in the submillimeter range, we cannot place constraints on the dust properties.

The derived dust temperatures (see Table 2) lie between 11.6 and 21.3 K, approximately in the same range as the far-infrared color temperatures from ISO and IRAS fluxes of the whole regions (see Table 1). In comparison to other studies, the values are consistent with those of cold dust components derived and assumed for young dense clumps (e.g. Beuther & Steinacker 2007; Sridharan et al. 2005; Enoch et al. 2007).

The estimated masses that reside in these cold dust and gas components range from 2 $M_\odot$ up to 166 $M_\odot$. Taking the mass estimates at face value, four of the clumps may be massive enough (>100 $M_\odot$) to form a high-mass star and an accompanying cluster, if one assumes that a fraction of 10% of the total mass ends up in massive stars (Zinnecker & Yorke 2007). The star formation efficiency is observationally not well-constrained on the scales of individual clumps.

From the source sizes in Table 2, volume-averaged densities were derived for our clump sample under the assumption of spherical symmetry. The resulting densities are $4 \times 10^4\,\mathrm{cm}^{-3} < n_{\mathrm{H}_2} < 10^6\,\mathrm{cm}^{-3}$ with a median value of $2 \times 10^5\,\mathrm{cm}^{-3}$. Compared to studies of dense condensations found in IRDCs (Rathborne et al. 2006, median density $3 \times 10^4\,\mathrm{cm}^{-3}$) and in Cygnus X (Motte et al. 2007, median density $2 \times 10^5\,\mathrm{cm}^{-3}$), the evaluated clumps seem to be more similar to the latter sample based on a millimeter continuum survey. Both the mentioned samples seem to contain candidate objects representing very early stages of massive star formation (e.g. massive infrared-quiet cores). For the sample of Beuther et al. (2002) based on IRAS measurements and containing luminous infrared sources, a lower mean density of $9 \times 10^3\,\mathrm{cm}^{-3}$ is recalculated in Motte et al. (2007). The direct comparison of these densities may be affected by systematically different derivation methods, but it suggests that the source selection based on longer wavelengths gives access to presumably less evolved sources. In the present case, the 170 μm band measurements constrain the average dust temperature to lower values than those that can be inferred from the IRAS bands.

5.2. The nature of the 24 μm sources

The majority of the clumps appear in a stage where 24 μm sources are present. In the following we discuss their ability to generate high-mass star progenitors and then evaluate selected

Table 3. Results of the SED fitting for three very red young stellar objects.

Region ISOSS…	J19357+1950	J20153+3453	J20298+3559
Source	5	2	–
Associated clump	SMM2	SMM1	SMM1
Selected cut-off	$\chi^2_\mathrm{d} < 14.2$	$\chi^2_\mathrm{d} < 9.3$	$\chi^2_\mathrm{d} < 12.5$
Fitted models	Stage I	Stage I	Stage I
Total extinction	$A_\mathrm{V} \sim 85$	$A_\mathrm{V} \sim 100$	$A_\mathrm{V} > 200$
Central mass ($M_\odot$)	0.2–2.1	0.7–2.3	0.2–4.6
Envelope accretion rate ($M_\odot$/yr)	1.6×10^{-6}–8.9×10^{-5}	1.5×10^{-6}–3.4×10^{-4}	4×10^{-6}–7×10^{-4}

subsamples in more detail. During their formation high-mass stars develop high luminosities. According to the approach of McKee & Tan (2003), values above 100 $L_\odot$ are already reached when one solar mass has been accreted. The corresponding timescale is around several 10^4 years. Therefore young high-mass stars should stand out as luminous sources. However, due to the reprocessing of the radiation at short wavelengths by the surrounding dusty envelopes, only a fraction of the luminosity is released at the infrared wavelengths we probed (here we consider $\lambda \leq 24\,\mu$m). If the source is deeply embedded, we expect its infrared colors to be very red and the emission at optical wavelengths to be undetectable. By combining the classification from the colors with an estimate of the total luminosity including the far-infrared and submillimeter data, we therefore get a handle on the probability of a source being a high-mass star precursor. Sources of Stage II or later should generate high luminosities to be considered candidate massive YSOs.

We consider the sources' locations in the infrared color-color space as qualitatively describing their evolutionary stages. From the sample of 24 μm sources that has been evaluated in the Analysis section the majority is estimated to be comparable to Stage II models. As the majority of the associated clumps do not substantially exceed a total luminosity of 200 $L_\odot$, we consider most of these objects as being rather low-mass YSOs. Their association with the submillimeter clumps suggests that they have formed inside and that the clumps contain density substructures.

5.2.1. Very red protostar candidates

As described above, sources that display very red infrared colors and sources that are not detected in the shorter-wavelength bands are the best candidates to represent very young objects that may evolve to massive YSOs. Using Fig. 11 we selected Source 5 in ISOSS J19357+1950, Source 1 in ISOSS J19486+2556, and Source 2 in ISOSS J20153+3453. The remaining sources with [8]–[24] > 5 are not associated with massive submillimeter clumps and probably will not be able to accrete enough material to end up as high-mass stars. Furthermore, the submillimeter source SMM1 in ISOSS J20298+3559 was found in Krause et al. (2003) to be a candidate Class 0 object. We detected a 24 μm source towards this peak, which is not seen at shorter wavelengths. Associated outflow-tracing emission supports its classification as young protostellar object.

Source 5 in ISOSS J19357+1950 is located towards the massive clump SMM2. We applied the online model fitter using the fluxes including upper limits in the H band, at 70, 450, and 850 μm. Source 2 found towards the massive clump ISOSS J20153+3453 SMM1 exhibits very red colors and is associated with a possible outflow. The online model fitter was fed with the fluxes including upper limits in the J band, at 70, 450, and 850 μm. For SMM1 in ISOSS J20298+3559, we input the fluxes measured at 24, 70, 450, and 850 μm and upper limits in the IRAC bands and in the Ks band. The range of possible foreground extinction was selected to $A_\mathrm{V} \leq 500$. The fitting results for these three sources are listed in Table 3. From the inspection of the SED plots, we established a cut-off value of χ^2_d (χ^2 per datapoint) to select the models that fit the datapoints within reasonable margins. We also give the total extinction to the central source by combining the fitted foreground extinction with the extinction along the line of sight from the model outer radii inwards. These parameters are degenerate to some extent and allow models with different envelope sizes to be fitted via compensating foreground extinctions. The results are consistent with the interpretation of the sources as young embedded stellar precursors. The observed outflow activity signatures accord with high accretion rates for the last two sources. In the cases of ISOSS J19357+1950 SMM2 and ISOSS J20153+3453 SMM1, the estimated high total masses of around 100 $M_\odot$ residing in cold components of dust and gas should allow ongoing accretion and the build-up of high-mass stars. However, due to the multiplicity of near-infrared sources that are detected in the vicinity of ISOSS 20153+3453 SMM1, the further evolution of this object is not straightforward. Towards ISOSS J19357+1950 SMM2, there also is a second, more evolved source nearby. In the third case, the mass estimate of about 10 $M_\odot$ for ISOSS J20298+3559 SMM1 is consistent with the source being an intermediate-mass star precursor.

The remaining very red, candidate Stage I source located towards the clump SMM1 in the region ISOSS J19486+2556 is particularly interesting because of the low infrared luminosity in comparison to the submillimeter, making it a candidate for a young and deeply embedded object. We input the photometric data into the online model fitter including upper limits in the Ks band, at 70, 450, and 850 μm. We chose a cut-off at $\chi^2_\mathrm{d} < 49.6$ to select the acceptable fits. The results for this source are ambiguous. Among the selected models are several belonging to the Stage I category with central source masses of about 0.1 $M_\odot$ but also a majority of Stage II models with central source masses between 3 and 4.5 $M_\odot$, both with and without envelopes. There is no significant difference in the fitted total extinction towards the central sources. We therefore cannot assess and constrain the parameters of this source.

5.2.2. Evolved young stellar objects

We also detected sources whose SEDs are dominated by emission at mid-infrared wavelengths that exhibit higher total luminosities and may represent more massive YSOs. By comparing the spectral energies at 24 μm and 70 μm, we found two candidate sources, located towards SMM4 in ISOSS J20298+3559

Table 4. Results of the SED fitting for two evolved young stellar objects.

Region ISOSS…	J20298+3559	J22478+6357
Source	8	3
Associated clump	SMM4	SMM1 East
Selected cut-off	$\chi^2_\mathrm{d} < 3.3$	$\chi^2_\mathrm{d} < 2.1$
Fitted models	Stage II[a]	Stage II[b]
Total extinction	$6 < A_\mathrm{V} < 9.4$	$29 < A_\mathrm{V} < 41$
Total luminosity ($L_\odot$)	~150	~2000
Central mass ($M_\odot$)	3.2–4.9	6–8.5
Preferred inclination	low	–
Disk mass ($M_\odot$)	4×10^{-6}–10^{-1}	10^{-5}–10^{-1}
Accretion rate ($M_\odot$/yr)	10^{-11}–10^{-6}	5×10^{-11}–2×10^{-5}
System age (yr)	10^6–10^7	10^6–6×10^6

[a] $M_\mathrm{disk}/M_* \geq 7.7 \times 10^{-7}$; [b] $M_\mathrm{disk}/M_* \geq 9.5 \times 10^{-7}$.

(Source 8) and SMM1 East in ISOSS J22478+6357 (Source 3). We also used the fluxes from Krause et al. (2003, IRS 6) for the *I*, *J*, *H*, and *K*s bands as well as upper limits at 70, 450, and 850 μm for the former and upper limits in the *J* band, at 70, 450 and 850 μm for the latter source. The fitting results are compiled in Table 4. We consider the first source to be an embedded proto- or pre-main-sequence star of intermediate mass as also suggested by Krause et al. (2003). It was probably formed in the SMM4 clump. The results for the second source are consistent with the source representing an evolved YSO of at least intermediate mass that is still embedded and presumably has been formed within the clump SMM1 East.

6. Conclusions

We have analyzed multi-wavelength observations of five starforming regions that were identified using the ISOPHOT Serendipity Survey at 170 μm. From the discussed results we infer:

1. We found one to four compact (~0.2 pc) submillimeter condensations in every region, which represent molecular clumps containing a cold component of gas and dust. The dust temperature estimates vary between 11.6 and 21.3 K and accord with the large-scale color temperatures measured in the far-infrared.
2. The resulting estimated clump masses that reside in these cold components range from 2 to 166 $M_\odot$. Four out of twelve clumps may be massive enough (>100 $M_\odot$) to be promising as birthplaces for high-mass stars.
3. We identified multiple associated mid-infrared sources for the majority of the clumps, suggesting that they embody significant density substructures on smaller scales than probed by the submillimeter observations ($\gtrsim$0.1 pc). Since the emission of most clumps is dominated by the cold material, we expect thriving star formation from further collapse of overdensities.
4. Most of the associated sources are considered as low-mass YSOs in an evolutionary state later than Class 0/I partly embedded in the clumps where they have formed.
5. In the region ISOSS J19357+1950, we found a massive clump of around 100 $M_\odot$. A probably deeply embedded accreting Class 0/I protostar of ~1 $M_\odot$ is detected adjacent to a more evolved YSO. Similarly, one massive clump of about 100 $M_\odot$ is present in ISOSS J20153+3453 and a cluster of sources is detected in the vicinity that contains a presumably deeply embedded accreting protostar with a current mass of ~1.5 $M_\odot$. Its evolutionary state corresponds to Class 0/I, and there is evidence of outflow activity from this object.
6. The source SMM1 in ISOSS J20298+3559 probably represents a young accreting intermediate-mass star precursor embedded in a molecular clump of ~10 $M_\odot$. Towards SMM4 in the same region we identified an embedded proto- or pre-main-sequence star of 3.2–4.9 $M_\odot$ that probably evolved from the associated clump of ~60 $M_\odot$.
7. In the region ISOSS J22478+6357, a candidate protostar of 6–8.5 $M_\odot$ is found that is embedded in the associated SMM1 East clump (~60 $M_\odot$).
8. We do not detect stellar precursors that could have current masses of 10 $M_\odot$ or more. Therefore we cannot be sure whether such objects will emerge within the identified clumps. However, the presence of intermediate-mass proto- or pre-main-sequence star candidates and the large clump masses indicate that one can expect that high-mass stars are also formed in these systems.
9. Our study reveals that the search for regions containing large fractions of cold material in the far-infrared has successfully identified starforming regions associated with cold and massive clumps. Compared to sources selected at shorter wavelengths they may represent less evolved stages of high-mass star formation, and in that respect, substantial impact can be expected from future (space) missions like Herschel and Planck. Furthermore, this study demonstrates that the detailed starforming content can only be accessed with a multi-wavelength approach including sensitive mid- and far-infrared observations.

Acknowledgements. Based on observations with ISO, an ESA project with instruments funded by ESA Member States (especially the PI countries: France, Germany, the Netherlands, and the UK) and with the participation of ISAS and NASA. The ISOSS was supported by funds from the DLR, Bonn. Based on observations collected at the Centro Astronómico Hispano Alemán (CAHA) at Calar Alto, operated jointly by the Max Planck Institut für Astronomie and the Instituto de Astrofísica de Andalucía (CSIC), and on observations with the James-Clerk-Maxwell Telescope (JCMT), as well as on observations made with the Spitzer Space Telescope, which is operated by the Jet Propulsion Laboratory, California Institute of Technology under a contract with NASA. This publication makes use of data products from the Two Micron All Sky Survey, which is a joint project of the University of Massachusetts and the Infrared Processing and Analysis Center/California Institute of Technology, funded by the National Aeronautics and Space Administration and the National Science Foundation. The Digitized Sky Surveys were produced at the Space Telescope Science Institute under US Government grant NAG W-2166. The Second Palomar Observatory Sky Survey (POSS-II) was made by the California Institute of Technology with funds from the National Science Foundation, the National Geographic Society, the Sloan Foundation, the Samuel Oschin Foundation, and the Eastman Kodak Corporation. M.H. thanks Jürgen Steinacker and Ulrich Klaas (both at MPIA) for their support and helpful discussions, and Kalevi Mattila and José Gonçalves (University of Helsinki Observatory) for hospitality and fruitful comments.

References

André, P. 1994, in The Cold Universe, ed. T. Montmerle, C. J. Lada, I. F. Mirabel, & J. Tran Thanh van, 179
Baumeister, H., Bizenberger, P., Bayler-Jones, C. A. L., et al. 2003, in Instrument Design and Performance for Optical/Infrared Ground-based Telescopes, ed. M. Iye, & A. F. M. Moorwood, Proc. SPIE, 4841, 343
Beichman, C. A., Neugebauer, G., Habing, H. J., Clegg, P. E., & Chester, T. J. 1988, Infrared astronomical satellite (IRAS) catalogs and atlases, Explanatory supplement, Vol. 1
Beuther, H., & Steinacker, J. 2007, ApJ, 656, L85
Beuther, H., Schilke, P., Menten, K. M., et al. 2002, ApJ, 566, 945
Beuther, H., Churchwell, E. B., McKee, C. F., & Tan, J. C. 2007, in Protostars and Planets V, ed. B. Reipurth, D. Jewitt, & K. Keil, 165
Birkmann, S. M., Krause, O., & Lemke, D. 2006, ApJ, 637, 380
Birkmann, S. M., Krause, O., Hennemann, M., et al. 2007, A&A, 474, 883

Bizenberger, P., McCaughrean, M. J., Birk, C., Thompson, D., & Storz, C. 1998, in Infrared Astronomical Instrumentation, ed. A. M. Fowler, & A. M. Fowler, Proc. SPIE, 3354, 825

Bogun, S., Lemke, D., Klaas, U., et al. 1996, A&A, 315, L71

Brand, J., & Blitz, L. 1993, A&A, 275, 67

Draine, B. T., & Lee, H. M. 1984, ApJ, 285, 89

Engelbracht, C. W., Blaylock, M., Su, K. Y. L., et al. 2007, PASP, 119, 994

Enoch, M. L., Glenn, J., Evans, II, N. J., et al. 2007, ApJ, 666, 982

Fazio, G. G., Hora, J. L., Allen, L. E., et al. 2004, ApJS, 154, 10

Gordon, K. D., Engelbracht, C. W., Fadda, D., et al. 2007, PASP, 119, 1019

Holland, W. S., Robson, E. I., Gear, W. K., et al. 1999, MNRAS, 303, 659

Indebetouw, R., Mathis, J. S., Babler, B. L., et al. 2005, ApJ, 619, 931

Indebetouw, R., Robitaille, T. P., Whitney, B. A., et al. 2007, ApJ, 666, 321

Jenness, T., & Economou, F. 1999, in Astronomical Data Analysis Software and Systems VIII, ed. D. M. Mehringer, R. L. Plante, & D. A. Roberts, ASP Conf. Ser., 172, 171

Jenness, T., & Lightfoot, J. F. 1998, in Astronomical Data Analysis Software and Systems VII, ed. R. Albrecht, R. N. Hook, & H. A. Bushouse, ASP Conf. Ser., 145, 216

Kessler, M. F., Steinz, J. A., Anderegg, M. E., et al. 1996, A&A, 315, L27

Krause, O. 2003, Ph.D. Thesis, Combined Faculties for the Natural Sciences and for Mathematics of the Ruperto-Carola University of Heidelberg, Germany

Krause, O., Lemke, D., Tóth, L. V., et al. 2003, A&A, 398, 1007

Krause, O., Vavrek, R., Birkmann, S., et al. 2004, Balt. Astron., 13, 407

Lemke, D., Klaas, U., Abolins, J., et al. 1996, A&A, 315, L64

Low, F. J., Smith, P. S., Werner, M., et al. 2005, ApJ, 631, 1170

Makovoz, D., & Marleau, F. R. 2005, PASP, 117, 1113

McKee, C. F., & Tan, J. C. 2003, ApJ, 585, 850

Motte, F., Bontemps, S., Schilke, P., et al. 2007, A&A, 476, 1243

Ossenkopf, V., & Henning, T. 1994, A&A, 291, 943

Rathborne, J. M., Jackson, J. M., & Simon, R. 2006, ApJ, 641, 389

Rathborne, J. M., Simon, R., & Jackson, J. M. 2007, ApJ, 662, 1082

Rawlings, M. G., Juvela, M., Mattila, K., Lehtinen, K., & Lemke, D. 2005, MNRAS, 356, 810

Reach, W. T., Rho, J., Young, E., et al. 2004, ApJS, 154, 385

Reach, W. T., Megeath, S. T., Cohen, M., et al. 2005, PASP, 117, 978

Rieke, G. H., Young, E. T., Engelbracht, C. W., et al. 2004, ApJS, 154, 25

Robitaille, T. P., Whitney, B. A., Indebetouw, R., & Wood, K. 2007, ApJS, 169, 328

Robitaille, T. P., Whitney, B. A., Indebetouw, R., Wood, K., & Denzmore, P. 2006, ApJS, 167, 256

Sandell, G., & Weintraub, D. A. 2001, ApJS, 134, 115

Sault, R. J., Teuben, P. J., & Wright, M. C. H. 1995, ASP Conf. Ser., 77, 433

Shepherd, D. S., Povich, M. S., Whitney, B. A., et al. 2007, ApJ, 669, 464

Sridharan, T. K., Beuther, H., Saito, M., Wyrowski, F., & Schilke, P. 2005, ApJ, 634, L57

Sridharan, T. K., Beuther, H., Schilke, P., Menten, K. M., & Wyrowski, F. 2002, ApJ, 566, 931

Stickel, M., Krause, O., Klaas, U., & Lemke, D. 2007, A&A, 466, 1205

Tody, D. 1993, in Astronomical Data Analysis Software and Systems II, ed. R. J. Hanisch, R. J. V. Brissenden, & J. Barnes, ASP Conf. Ser., 52, 173

Werner, M. W., Roellig, T. L., Low, F. J., et al. 2004, ApJS, 154, 1

Whitney, B. A., Wood, K., Bjorkman, J. E., & Wolff, M. J. 2003, ApJ, 591, 1049

Zinnecker, H., & Yorke, H. W. 2007, ARA&A, 45, 481